Suppression of the commensurate magnetic phase in nanosized hübnerite $MnWO_4$

P. Zajdel,[1] A. Gągor,[2,*] D. M. Pajerowski,[3] M. Ptak,[2] and M. Szlawska[2]

[1]*Institute of Physics, University of Silesia, ul. Uniwersytecka 4, 40-007 Katowice, Poland*

[2]*Institute of Low Temperature and Structure Research, Polish Academy of Sciences, P.O. Box 1410, 50-950 Wrocław 2, Poland*

[3]*Quantum Condensed Matter Division, Oak Ridge National Laboratory, Oak Ridge, Tennessee 37831, USA*

(Received 19 November 2016; revised manuscript received 2 April 2017; published 18 May 2017)

Magnetic structures of nanosized (20 to 70 nm) powders of $MnWO_4$ and $MnWO_4$:Mo were studied using neutron powder diffraction (NPD). Sizes and shapes of the crystallites calculated from anisotropic peak broadening of diffraction peaks were found to be orthogonal parallelepipedlike with the longest edge along the c axis and the shortest along the b axis. SQUID measurements indicate the presence of two magnetic transitions around 8 and 12 K. Rietveld refinement of the NPD data below the magnetic transition was consistent with the presence of an incommensurate spiral-like (ac-AF2) phase. A commensurate phase AF1 was not observed down to 2.5 K for all of the samples.

DOI: 10.1103/PhysRevB.95.174427

I. INTRODUCTION

$MnWO_4$ is a type-II multiferroic [1] as the ferroelectricity (FE) appears together with an incommensurate (IC) magnetic structure [2–5]. The onset of the cycloid structure alone is not enough to break the inversion symmetry of the system [6,7] and one must consider additional effects like a competition between Dzyaloshinskii-Moriya [8,9] and isotropic exchange interactions, which result in a complicated and delicate balance of the system [10].

Hübnerite $MnWO_4$ has been reported to crystallize in a centrosymmetric monoclinic $P2/c$ space group with lattice parameters $a = 4.82$ Å,$b = 5.75$ Å,$c = 4.99$ Å,$\beta = 91.07$ [2]. However, recently the space group has been verified using single-crystal neutron and x-ray diffraction [11] to be noncentrosymmetric and polar $P2$ as evidenced by the appearance of $(h0l)\,l =$ odd reflections forbidden in $P2/c$. The main structural effect of lowering the symmetry is a shift of two previously coupled Mn ions along the b axis, opposite to W and O. The crystal structure is built of quasi-1D zigzag chains of edge-sharing Mn octahedra (Fig. 1) propagating along the c axis. The closest distances between Mn ions are: in-chain in the bc plane (3.26 Å), interchain along the b axis (4.44 Å), and interchain along the a axis (4.82 Å).

Without an external magnetic field, there are three magnetic phases reported for $MnWO_4$ [2,12]. At the lowest temperatures, below $T1 \approx 8$ K, a collinear and commensurate antiferromagnetic ordering (AF1) is observed with the propagation vector $k = (-1/4, 1/2, 1/2)$. Upon heating above 8 K, the propagation vector becomes incommensurate $k = (-0.214, 1/2, 0.457)$ with magnetic moments forming a cycloid with components along all crystallographic directions (IC AF2). The structure remains incommensurate up to the transition to the paramagnetic phase at $T3 = 13.5$ K but at $T2 \approx 12.3$ K a new sinusoidally modulated phase appears (IC AF3), with no magnetic moment along the b axis. The AF2 phase has been shown to be multiferroic and application of an electric field was used to drive the system into a magnetic domain with the single chiral character [13,14].

All of the magnetically ordered phases display a weak structural modulation [15] that can be connected with the magnetic modulation vector through the superspace approach [16]. However, for neutron scattering interrogation of the magnetic structure, the original monoclinic group is sufficient to model the nuclear structure and was used in this paper.

Low temperatures of the transitions and long times of FE domain reorientation [17] make manganese tungstate a poor candidate for multiferroic devices. However, $MnWO_4$ still has technological potential at ambient temperatures, for example in humidity sensors, and efforts have been made to increase the active surface by varying crystallite size [18,19], changing morphology [20], or doping [21,22].

At the same time, magnetic measurements and vibrational spectroscopy of the nanosized materials [4,23] reveals significant changes in the magnetic behavior of the system. Instead of well-defined transitions, the magnetization curve develops a broad hump and a plateau (Fig. 4 in [23]) in the temperature region where the IC AF3 and IC AF2 phases were observed in a bulk form (Fig. 3 in [4]). Additionally, a different magnetization trend appeared in the temperature range of the AF1 phase. Recently a single transition at 6 K in nanosized $MnWO_4$ was also observed by Ungelenk *et al.* [24].

The inability to separately resolve the AF3 and AF2 phases may be due to size dispersion in the nanoparticle samples or structural disorder. The single ion anisotropy was singled out as an important factor in explaining trends observed in the transition temperatures upon substitution on manganese site [21,25]. For example, adding 10% of Fe suppressed the IC AF2 phase in favor of commensurate, collinear AF1 [26], while 5% of Co expanded IC AF2 down in temperature [21]. Local irregularities, in part caused by an increased surface to volume ratio of the grain, disturb a local anisotropy field, which was pointed out as the main factor behind the confinement of the magnetic moment in the ac plane of the IC AF3 phase [4]. Terminal surface spins, which are more numerous in smaller samples, experience a different anisotropy than those in the bulk of the sample, interrupting the bulk behavior. In essence, the decrease of the anisotropy that confines the magnetic moment in the IC AF3 phase to the ac plane should cause an expansion of the temperature range of the IC AF2 phase with magnetic moment along the b axis.

*a.gagor@int.pan.wroc.pl

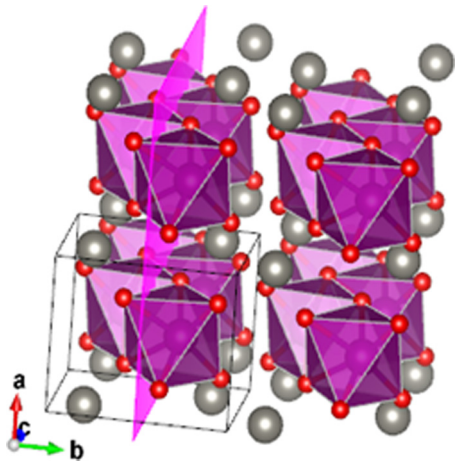

FIG. 1. Crystal structure of $MnWO_4$ with one of the (010) planes highlighted.

In order to verify the character of the long range order and investigate the coupling between magnetic and structural properties of nanocrystalline $MnWO_4$, three samples differing in domain size and composition were synthesized using the sol-gel method described previously by Maczka *et al.* [18]. An attempt to increase local strain and promote anisotropy disorder was made by substituting tungsten with nominally 15% molybdenum. The addition of Mo in the bulk form has been investigated earlier by Meddar *et al.* [22] and has been shown to slightly raise the transition temperatures.

As the stability and existence of the AF2 phase are critical for understanding the multiferroic properties of $MnWO_4$, a neutron powder diffraction study of the long magnetic order was carried out to get insight into coupling between magnetic and electric properties of the system. The sensitivity of the NPD to both structural and magnetic orders shall also bring insight into the rapid increase of magnetization below 5 K observed in the nanosized material [23], which may indicate the presence of a ferromagnetic component or Curie-like disordered paramagnetic moments.

II. MATERIALS AND METHODS

The three samples (S1, S2, and S3) used for this study were synthesized following a previously reported method [18]. The size of the grains was controlled by the temperature of the synthesis, which was chosen to be 130 °C (403 K) for sample S1 and 230 °C (503 K) for samples S2 and S3. Additionally, the targeted composition of S3 aimed at substituting tungsten with a 15% molar fraction of molybdenum. The masses of the samples were around 2 g for S1 and S2, and 1 g for S3.

The synthesis yielded single phase materials and the quality of the samples S2 and S3 was verified using powder XRD using a Cu $K\alpha$ source. The Rietveld [27] method was applied to refine collected patterns using Fullprof [28] software. As the width of the diffraction peaks was larger than the machine broadening, size and strain models appropriate for Laue class $2/m$ (size = 15, strain = 2) were used with the Thompson-Cox-Hastings peak profile [29]. The anisotropic strain broadening was introduced in the quartic form [30]. The anisotropic Lorentzian (Scherrer) size broadening was modeled using the spherical harmonic formalism developed by Jarvinen [31]. The machine resolution profile was obtained from a silicon standard. In all cases, ionic atomic form factors for Mn^{2+}, W^{6+}, Mo^{6+}, and O^{2-} were used.

Neutron scattering experiments were performed at the NIST Center for Neutron Research, Gaithersburg, MD, USA. The samples were loaded in a He dry glovebox into vanadium cans 50 mm long and 6 mm in diameter for the sample S3 and 9.2 mm in diameter for the samples S2 and S1.

The temperature dependencies of the order parameters were measured on a cold neutron triple-axis spectrometer NG5 (SPINS). The experimental setup and neutron beam path consisted of 37′ (minutes of arc) in-pile collimation, PG(002) LN_2 cooled filter, 80′ radial collimator, the sample, another 80′ radial collimator, second Be LN cooled filter, and multiblade analyzer in a flat mode. The selected wavelength was 4 Å ($E_i = E_f = 5$ meV).

The high-resolution neutron powder diffraction data were collected using the BT-1 32 detector neutron powder diffractometer. A Ge(311) monochromator with a 75° take-off angle, $\lambda = 2.0780(2)$ Å, and in-pile collimation of 60′ were used. Data were collected over the 2θ range of 1.3°−166.3° with a step size of 0.05°. The instrumental resolution was obtained from the Al_2O_3 data available from the instrument page (http://ncnr.nist.gov/instruments/bt1/alumina.html). The scattering lengths used in the refinement were (in fm) Mn = −3.73, W = 4.86, Mo = 6.715, O = 5.803. The magnetic phase was treated using the irreducible representation of the propagation vector group formalism [32]. Initial analysis and basis vectors were prepared using SARAh software [33,34]. The visualization of the structures was done using VESTA package [35]. Diffractograms were collected at the following temperatures: 4.7 K for S1; 2.8, 9, and 20 K for S2; 5 and 20 K for S3. Impurity peaks at 53.33°($d = 2.31$ Å) and 58.15°($d = 2.137$ Å) in diffractograms collected for S1 and S3 are connected with unmasked sample environment.

Bulk magnetization measurements were performed in a dc mode using Quantum Design MPMS system in the ILTSR PAS, Wroclaw, Poland.

III. RESULTS

A. XRD

Samples S2 and S3 were tested by room temperature XRD. The diffractograms and refinement results are reported in Table I of the Supplemental Material (SM) [34].

B. Bulk magnetization

A low-temperature section of magnetization measured for samples S2 and S3 is presented in Fig. 2. In the case of the undoped sample, one can identify a broad transition at around 6 K which is suppressed by application of magnetic field. Similar behavior was observed in [24], where the application of a magnetic field lowered the susceptibility. The 6 K transition is also slightly suppressed without an increased field for Mo-doped sample S3. For both S2 and S3, there is a small hump around 13 K, which indicates a possible transition to an ordered state.

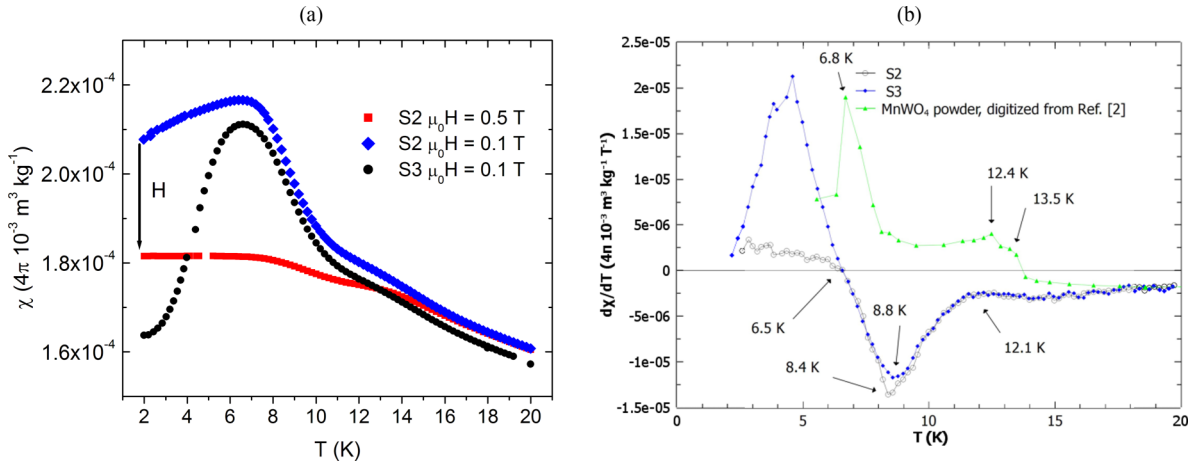

FIG. 2. (a) Magnetization curves reveal a broad transition at around 6 K and small hump around 14 K. (b) Comparing the derivative to a digitization of the bulk powder shows a smearing of the ordering feature and a change in the $T1$ transition character. The transition near 8 K, T^*, is found to be related to a change in spiral ellipticity that is seen in the neutron diffraction.

C. Cold neutron diffraction

Low-temperature measurements were performed over a 2θ range 25° to 45°, covering a region of two groups of magnetic peaks and one nuclear reflection. Peak M1 at around 30° originates from three ideally overlapping magnetic satellites $(000)^{+/-q}$ and $(010)^{-q}$. Peak M2 at around 34° consists of $(001)^{-q}$ and $(011)^{-q}$. The nuclear (N) reflection (010) is located at 41°. The splitting of M1 and M2 is characteristic of incommensurate phases AF2 and AF3. In the commensurate phase AF1, peaks M1 and M2 would unify into one peak at (1/4, 1/2, 1/2) within the experimental resolution, which is not the case.

The 2θ scans were merged into one data set and visualized using DAVE software [36]. The areas under the respective reflections were fit within the PAN module using a linear background and three Gaussians centered under M1, M2, and N.

In order to obtain a better estimate of the transition temperature, peak intensities were fit using an order parameter $y = y_0(T - T_N)^{2\beta}$ formula implemented in PAN (the intensity of a magnetic peak is proportional to the square of the magnetic moment, so the obtained exponent has to be divided by 2).

1. S1 (T_{synth} = 130 °C)

Temperature scans for S1 are presented in Fig. 3. The visible splitting of peaks M1 and M2 in Fig. 4 confirms an incommensurate character of the magnetic order which will be corroborated later in the article using thermal neutron diffraction.

Sample 1 was found to possess the weakest magnetic scattering despite its mass (2 g) being comparable to sample 2. Due to the limited number of measurements, the critical behavior was not fit to a power law, but linear fits of the data above 7 K and less than 10 K for M1 and M2 peaks give T_N values of 9.9 and 10.4 K, respectively.

2. S2 (T_{synth} = 230 °C)

The temperature scans for S2 are presented in Fig. 5 and there are no signs of commensurate order down to 2.5 K.

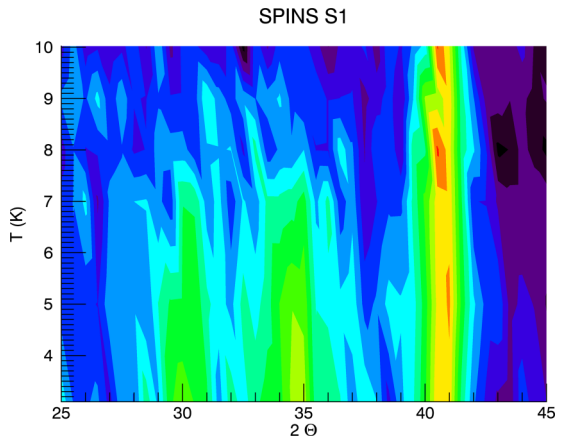

FIG. 3. Merged temperature scans of S1 show the robustness of the incommensurate phase down to the lowest measured temperature and the disappearance of the long range magnetic order at around 10 K.

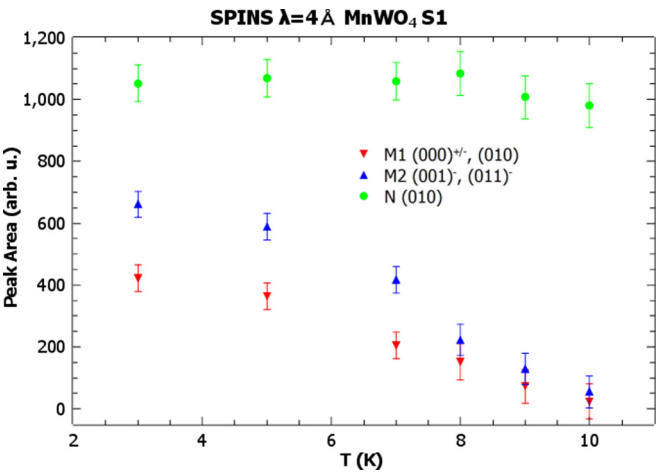

FIG. 4. Peak intensities (nuclear N green and magnetic peaks M1 red, M2 blue) shown are from fits to Fig. 3.

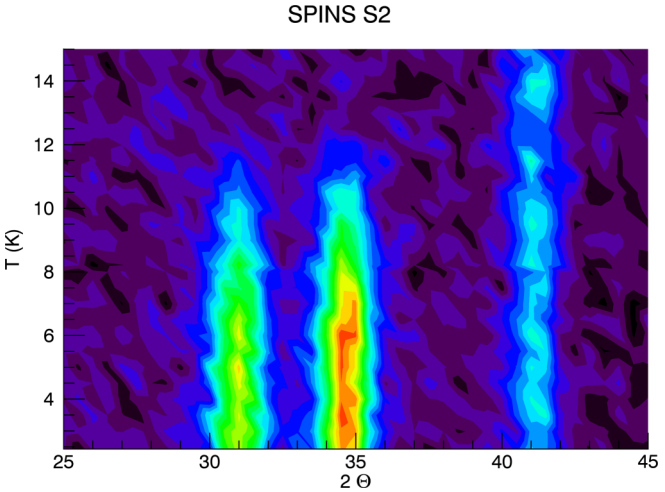

FIG. 5. Merged temperature scans of sample 2 revealed lack of commensurate phase AF1 and disappearance of the long range magnetic order at 12 K.

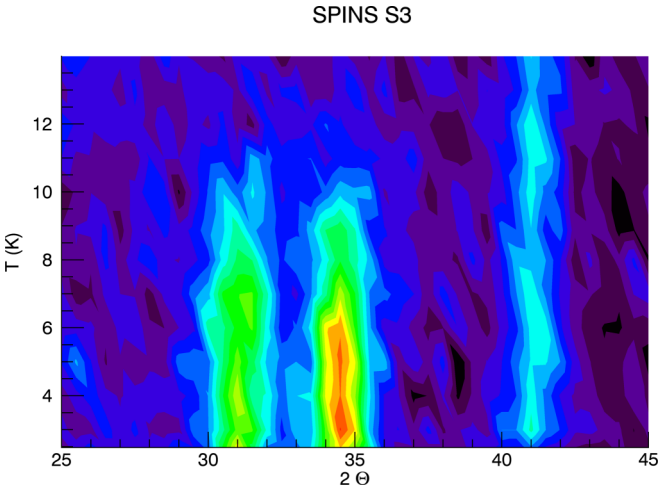

FIG. 7. Merged temperature scans of S3 revealed a lack of the commensurate phase AF1 and disappearance of the long range magnetic order at 12 K.

The area of the peaks extracted from the experimental data clearly revealed a notable discontinuity in intensity between 8.0 and 8.5 K, which indicated the possible presence of another transition, which is verified by comparison with thermal neutron data taken at 9 K.

The order parameter was fit in a temperature range 8.5-15 K closer to the visible transition Fig. 6.

The values of parameters extracted from the fits were: for peak M1 $T_N = 12.11(3)$ K,$2\beta = 0.53(22)$ and for peak M2 $T_N = 12.12(3)$ K,$2\beta = 0.41(17)$. The values in parentheses represent statistical uncertainty on a 1-σ level, so 12.12(3) is equivalent to 12.12 ± 0.03.

3. S3 (T_{synth} = 230 °C, Mo 15%)

A similar procedure was repeated for S3 and the results are presented in Figs. 7 and 8.

The attempt to fit critical behavior to intensities of magnetic peaks in the 8–14 K region gave: for peak M1 $T_N = 13.6(7)$ K, $2\beta = 0.34(9)$ and for peak M2 $T_N = 13.6(5)$K, $2\beta = 0.40(6)$. The lower value for exponent for peak M1 is probably caused by the outlier point at 12 K.

D. Thermal neutron diffraction

The cold neutron diffraction experiments display the absence of the commensurate AF1 phase due to the existence of two clear magnetic peaks (M1 and M2) at angles lower than the (010). In order to differentiate between AF2, with a finite b-axis moment, and AF3, without long-rage order along b, refinement of additional higher angle Bragg peaks is required.

1. S1 (T_{synth} = 130 °C)

The Rietveld refinement of the diffractogram collected at $T = 4.7$ K is presented in Fig. 9.

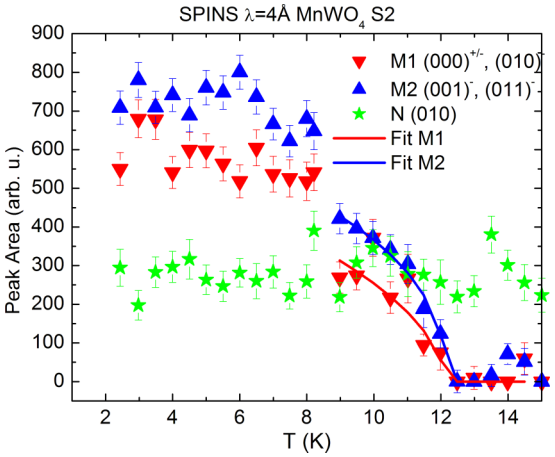

FIG. 6. Extracted peak intensities (nuclear N green and magnetic peaks M1 red, M2 blue) presented with fits of the order parameter in the 8.5–15 K region.

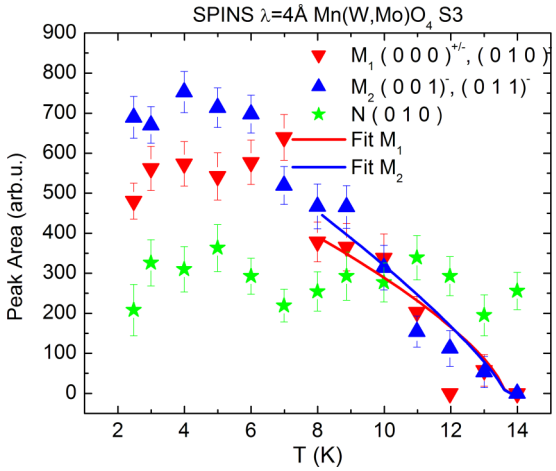

FIG. 8. Nuclear (N green) and magnetic peaks (M1 red, M2 blue) intensities obtained from fits for S3. Order parameter fits to magnetic peaks in the 8–14 K range give similar critical temperature $T_N = 13.6(7)$ K.

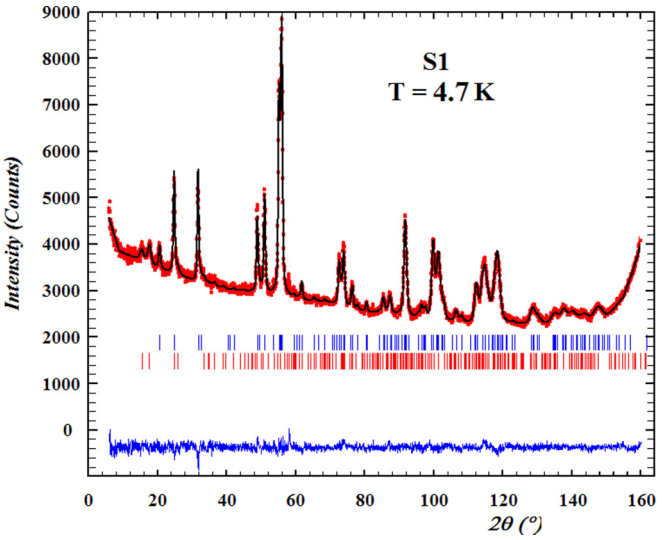

FIG. 9. Rietveld refinement of BT-1 data for S1. Blue vertical bars indicate the nuclear structure. Red verticals bars mark magnetic reflections.

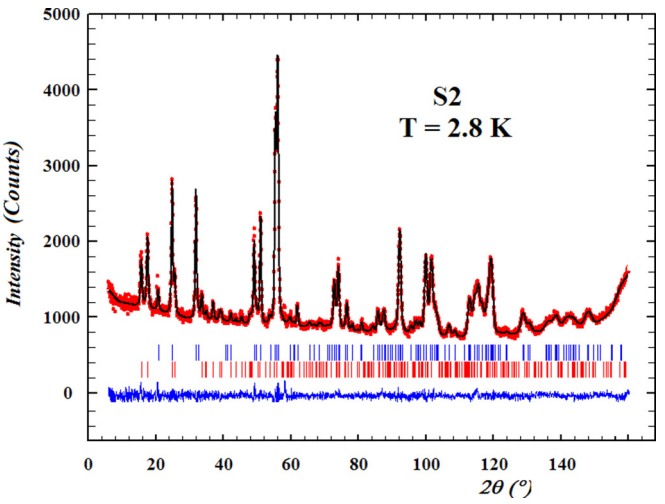

FIG. 10. Plot of the Rietveld refinement of the S2 at $T = 2.8$ K.

Refined structural parameters together with agreement factors $R_{\mathrm{Bragg}}(RB), R_{\mathrm{mag}}, \chi^2$ and background corrected R_p, R_{wp}, and R_{exp} are reported together with data for S3 in Table I.

S1 possesses the smallest magnetic moment located on Mn and the largest deviation from the commensurate propagation vector $\delta k = (0.048, 0, -0.061)$. Its crystallographic domain size is slightly smaller but comparable to S2 and S3 but the magnetic domain size of 7.0 nm is less than half of the respective size for S2 and S3. The anisotropy of the domain size was only refined for the crystallographic phase and the domain was largest along the c axis (36 nm) and shortest along the b axis (16 nm). Still, the smallest dimension of the crystallographic domain was over twice as large as the magnetic one indicating that the correlation length of the magnetic order was limited by an additional factor.

The refinement at 4.7 K revealed a nonzero magnetic component C2 along the b axis, which is in agreement with the presence of phase AF2. At the same time, S1 has the largest lattice parameters of all of the samples.

2. S2 ($T_{synth} = 230\,°C$)

The diffractograms for S2 were collected at 2.8 K (16 h), 9 K (5 h), and 20 K (5 h) (Fig. 10). The 2.8 and 9 K scans were

TABLE I. Structural parameters obtained from the NPD for S1 and S3 together with crystallographic (CD) and magnetic (MD) domain sizes. The CD values are reported as spherical average size and estimated anisotropy (in curly braces) and average sizes $H \times K \times L$ from widths of (100), (010), (002) reflections.

	S1 4.7 K	S3 5 K	S3 20 K
a (Å)	4.8205(2)	4.8156(1)	4.8164(2)
b (Å)	5.7749(2)	5.7610(2)	5.7612(3)
c (Å)	5.0210(2)	4.9986(2)	4.9991(2)
β (deg)	91.021(2)	91.035(2)	91.034(3)
y_{Mn}	0.6760(9)	0.6838(8)	0.6813(14)
y_{W}	0.1726(9)	0.1810(9)	0.1810(13)
x_{O1}	0.2200(6)	0.2146(7)	0.2130(9)
y_{O1}	0.1058(5)	0.1045(5)	0.1061(8)
z_{O1}	0.9391(5)	0.9417(5)	0.9425(8)
x_{O2}	0.2517(6)	0.2510(6)	0.2512(8)
y_{O2}	0.3776(7)	0.3760(7)	0.3762(11)
z_{O2}	0.3980(6)	0.3938(6)	0.3957(8)
B_{iso}	0.53(3)	0.41(3)	0.48(4)
qx, qz	−0.202(2), 0.4392(9)	−0.2140(5), 0.4550(3)	–
$C1$	3.3(2)	4.1(2)	–
$C2$	2.1(5)	2.7(4)	–
$C3$	0.7(3)	2.0(3)	–
Domain size CD	23{5}, 21 × 16 × 36	23{7}, 22 × 14 × 41	23{7}, 22 × 14 × 42
MD (nm)	7.0{−}	13{2}	–
$R_{\mathrm{Bragg}}, R_{\mathrm{mag}}, R_p,$	2.82, 7.36, 15.6,	3.02, 10.2, 15.6	5.17,–,22.4,
$R_{\mathrm{wp}}, R_{\mathrm{exp}}, \chi^2$	11.3, 10.93, 1.07	12.3, 12.45, 0.970	17.5, 19.13, 0.836

TABLE II. Comparison of Rietveld refinements performed on S2 at 2.8 and 9 K with and without a magnetic component along the b axis.

T	2.8 K		9 K	
Phase	AF2	AF3	AF2	AF3
$C1$, $C2$, $C3$	4.0(1), 3.5(2), 2.0(1)	5.1(1), 0, 2.2(2)	3.7(2), 2.6(3), 1.9(2)	4.3(1), 0, 2.1(2)
$R_{\text{Bragg}}, R_{\text{mag}}$	2.15, 5.19	2.36, 7.05	2.46, 10.5	2.58, 11.3
$R_{\text{wp}}, R_{\text{p}}, R_{\text{exp}}$	11.2, 13.6, 11.47	11.5, 14.0, 11.51	14.4, 18.2, 15.73	14.5,18.4,15.76
χ^2	0.985	1.030	0.863	0.868

used to verify the value of the moment along the b axis and explain a possible transition visible at 8.5 K in the cold neutron data. The first refinements for the S2 were performed assuming AF3 spin arrangement which consisted of components along a and c directions belonging to representation $\boldsymbol{\tau 2}$ (coefficients $C1$ and $C3$). To improve the initial fit a magnetic moment component $C2$ along the b axis belonging to $\tau 1$ was introduced in refinements (equivalent to phase AF2). Comparison of fits at 2.8 and 9 K (Table II) indicate that the AF2 phase gives a better result at both temperatures. In order to better estimate the stability of the AF2 solution, a series of fits with varying $C2$ was performed on the 2.8 K data set. Figure 11 clearly shows a well-established minimum at $C2 = 3.50$, which agrees well with the value 3.5(2) obtained from the free fit (Table II). In cases where $C2$ was constrained to 0, the convergence was achieved by a significant increase (from 4.0 to 5.0) of the parameter $C1$ with only a slight change in the parameter $C3$ (1.9 to 2.1), see inset in Fig. 11.

The final refinements for 2.8, 9, and 20 K scans were done with a refinement of anisotropic domain sizes, which improved the fits and are collected in Table III.

The incommensurate propagation vector of S2 has a smaller deviation $\delta k = (0.04, 0, -0.049)$ from the commensurate point $(-1/4, 1/2, 1/2)$ than for S1. This deviation slightly decreased with increasing temperature. The largest difference between 2.8 and 9 K data was observed in the value of the $C2$ component, which increased 20% from 2.9 to 3.6, when at the same time the $C1$ and $C3$ increased by less than 15%. This significant increase of $C2$ might be connected to the broad transition present in the SQUID (Fig. 2) data around 8 K and the sudden change in the magnetic intensity around 8 K visible in the cold neutron scans (Fig. 6).

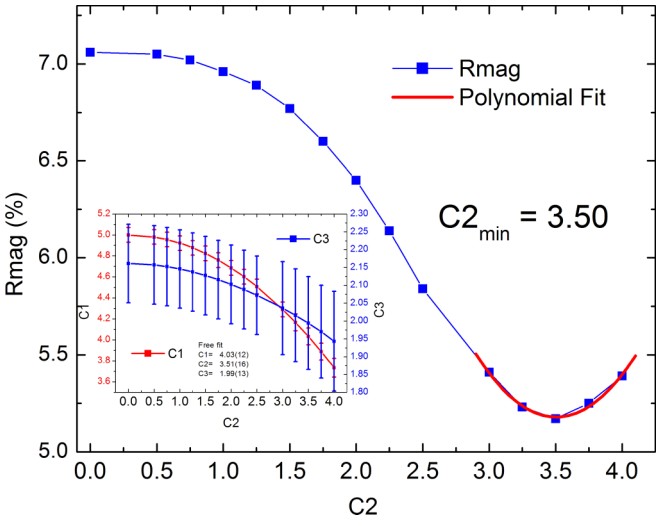

FIG. 11. Dependence of the agreement factor R_{mag} on the $C2$ coefficient that is proportional to the moment along the b axis. The inset shows a dependence of $C1$ (red) and $C3$ (blue) vs $C2$.

The refinement of the anisotropic crystallographic domain size gave a comparable result to those obtained from the XRD (see SM). The notable difference is a smaller size along the c axis 40 nm instead of 52 nm from the XRD. The magnetic domain size of 18 nm might be limited by the shortest dimension of crystallite along the b axis.

3. *S3 (T_{synth} = 230 °C, Mo 15%)*

Diffractograms for S3 were collected at 5 K (17 h) and 20 K (7 h) (Fig. 12). The deviation from the incommensurate propagation $\delta k = (0.036, 0, -0.045)$ is the smallest of all samples. The lattice parameters are shorter than for S1 at all temperatures. At 20 K the lattice parameter a is shorter but b and c are larger than the corresponding values for S2. Similar relation is observed between data at 5 K for S3 and 9 K for S2. The shortening of the unit cell along the a axis is expected due to a smaller ionic radius of Mo^{+6}(VI) 0.59 Å vs W^{+6}(VI) 0.60 Å [37], which is separating the MnO_6 layers along the a axis (Fig. 1). However, the overall cell volume at 20 K for S2 [$V = 138.566(7)$ Å^3] is smaller than for S3 $V = 138.692(11)$ Å^3. The crystallographic domain size $22 \times 14 \times 42$ nm^3 was comparable to the one obtained from the XRD with the exception of the c axis which was shorter (42 instead of 74 nm). Also, the magnetic domain size of 13 nm might be limited by the shortest crystallite dimension along the b axis equal to 14 nm.

IV. DISCUSSION

We have tested models for the magnetic structures of three nanosized $MnWO_4$ powder samples, checking the effects of finite size with two samples (S1 and S2) and the combination of finite size and Mo doping on the W site for a third sample (S3). While a polycrystalline synthesis has structural domains larger than 100 nm along the three crystallographic directions [18], the samples studied herein are less than 30 nm on their largest edge. The average crystallite sizes obtained from the anisotropic size broadening model implemented in Fullprof are similar for the XRD and NPD studies, and are summarized in Table IV. The synthesis dependent particle sizes are as expected from reported synthesis reports [18].

The nanoparticles were also found to have shape anisotropy. The analysis of the anisotropic character of the broadening performed in Fullprof indicated large size anisotropy in the

TABLE III. Structural parameters obtained from the NPD for S2. Parameters $C1$, $C2$, and $C3$ quantify magnetic moments along the main crystallographic directions. CD and MD are crystallographic and magnetic domain sizes, respectively (see caption of Table I).

	2.8 K	9 K	20 K
a (Å)	4.8187(1)	4.8187(2)	4.8197(2)
b (Å)	5.7560(2)	5.7552(2)	5.7559(2)
c (Å)	4.9947(1)	4.9954(2)	4.9958(2)
β (deg)	91.075(2)	91.081(2)	91.081(2)
y_{Mn}	0.6812(8)	0.6811(11)	0.6829(10)
y_W	0.1822(8)	0.1832(10)	0.1834(9)
x_{O1}	0.2137(6)	0.2138(8)	0.2148(7)
y_{O1}	0.1043(4)	0.1030(6)	0.1033(5)
z_{O1}	0.9430(4)	0.9432(6)	0.9438(6)
x_{O2}	0.2510(5)	0.2515(6)	0.2510(5)
y_{O2}	0.3757(6)	0.3758(8)	0.3757(7)
z_{O2}	0.3939(5)	0.3927(6)	0.3918(6)
B_{iso}	0.39(3)	0.35(4)	0.36(3)
qx, qz	−0.2102(2), 0.4513(2)	−0.2109(5), 0.4525(4)	–
$C1$	4.0(2)	3.5(3)	–
$C2$	3.6(2)	2.9(5)	–
$C3$	1.8(2)	2.1(4)	–
Domain size CD	27{6}, 28 × 19 × 40	28{5}, 28 × 20 × 40	28{5}, 28 × 20 × 38
MD (nm)	18{2}	15{2}	–
R_{Bragg}, R_{mag}, R_p,	2.10, 4.70, 13.4,	2.35, 10.0, 18.1,	2.84,–,20.4,
R_{wp}, R_{exp}, χ^2	11.2, 11.48, 0.97	14.4, 15.7, 0.856	14.8, 16.1, 0.906

RT XRD (see Table II in the SM). For example, the shape of the domain refined from the XRD for S2 is a regular parallelepiped with dimensions 27 × 19 × 52 nm^3, which is roughly consistent with average proportions of the whole grain reported earlier in SEM data (see Figs. 8 and 9 in [18]). The anisotropic crystallite sizes obtained from the NPD at temperatures 20 K and below are similar along the a and b axes but are shorter than the NPD refinements (50 nm XRD vs 40 nm NPD for S2) along the c axis (see Tables I and III). The origin of the difference between the c sizes of crystallites is unknown but it might be caused by simple mechanical fractures along the longest edge of the crystallite during transport and preparation.

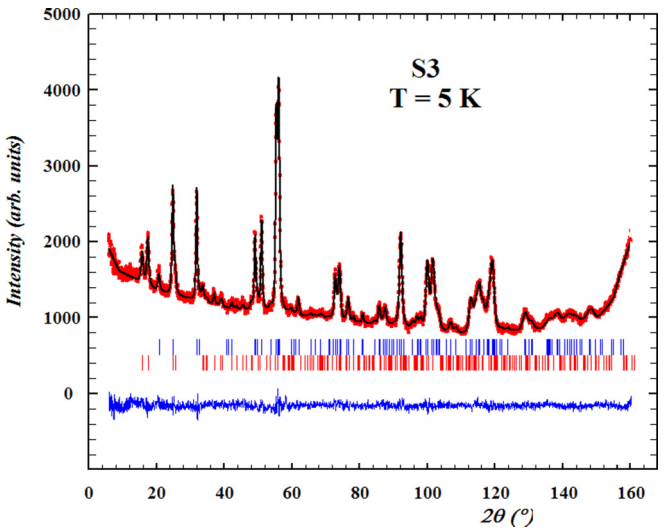

FIG. 12. A plot of the Rietveld refinement of the S3 at $T = 5$ K.

Finite strain was only seen with Mo doping, and not with simple size reduction. Biaxial strain components had to be included in the XRD refinements of S3, with the largest strain values in the ab plane. Such contribution to XRD lines was observed neither in S2 nor in the low temperature neutron refinements.

These samples follow the reported dependence of crystallographic parameters on sample size. At low temperatures, S1 had the largest lattice parameters, the smallest monoclinic angle, and the largest cell volume [139.754(6) Å^3 at 4.5 K], which was expected on the basis of its lowest synthesis temperature (130 °C) [18]. The unit cells of S2 [$V = 138.566(7)$ Å^3] and S3 [$V = 138.692(11)$ Å^3 at 20 K] have trend opposite to the one refined from the RT XRD where S2 was larger [$V = 139.062(5)$ Å^3] than S3 [$V = 138.749(7)$ Å^3] (Table I).

The cold neutron diffraction maps out the critical temperature of the onset of magnetic order (T_N). Reducing sample size was seen to reduce T_N, Table IV. The T_N of 13.6 K for Mo-doped S3 was slightly higher than 12.1 K for S2, which is in agreement with earlier observation for bulk material [22,38] where the addition of Mo raised the transition point. Due to large fitting uncertainties, the exact value of the order parameter could not be established but the values of β oscillate around 0.2, which is much lower than expected from mean field models. However, the expressions hold true for $T \rightarrow T_N^-$, so the reported critical exponents are not to be taken quantitatively, and it has been shown in single crystals that the interactions in $MnWO_4$ are highly three dimensional [10].

These SPINS data also showed the suppression of the commensurate AF1 and expansion of the incommensurate AF2/AF3 phase. The lack of AF1 is easy to identify as the (1/4, 1/2, 1/2) is absent and replaced by two offset peaks,

TABLE IV. The effect of particle size and Mo substitution on magnetic properties of $MnWO_4$.

	% Mo	T_{synth}(°C)	Domain size (nm)	T_N(K)	$T1$ (K)	T^* (K)	$\lvert m_{tot}\rvert$ (μ_B)
S1	0	130	23	10 ± 0.5	<2.5	6 ± 1	4.0 ± 0.4
S2	0	230	27	12.1 ± 0.1	<2.5	8.5 ± 0.5	5.8 ± 0.3
S3	15	230	23	13.6 ± 0.7	<2.5	7.5 ± 0.5	5.3 ± 0.3
Polycrystal (from Ref. [2])	0	800	>100	13.5	6.8	–	4.6[a]
Polycrystal (from Ref. [37])	15	1100	>100	14.6	<2	9.7	4.6

[a]This is from the AF1 base temperature, whereas at 9 K, 3.9 μ_B was seen at D1B on the polycrystal, which is comparable to the 4.9 μ_B seen on BT1 at 9 K for the nanoparticle S2.

Figs. 3, 5, and 7. This frailty of the AF1 state with respect to either impurities or decrease in size is not surprising, as in the initial neutron powder diffraction report there was already such an affect observed [2], whereby the transition from AF2 to AF1 decreased from 8 K in a single crystal to 6.8 K in a powder sample and Mn_3O_4 impurities were found to destroy the AF1 state. Various chemical dopings, such as Mo [38], have also been shown to modify the AF1/AF2 phase boundary.

The remaining question is the character of the incommensurate phase. Because of the reduced diffractogram quality of nanoparticles samples, we do not try to model the IC phase independently, but rather compare against existing works. The thermal neutron diffraction data collected at base temperatures (below 5 K) clearly show the presence of the magnetic moment along the b axis, pointing towards the AF2 phase, which came out as the best model for all magnetic refinements. The addition of the C2 component to the 9 K model for S2 (see Table II) lowered the R_{mag} from 11.3% to 10.5%. The same procedure for 2.8 K yielded a much better improvement of 7.05% to 5.19%, which is a notable difference. So, the T^* transition at around 8 K present in SQUID and SPINS data is likely to be connected with a modulation of the spiral ellipticity. A suppression of the AF1 phase replaced with a more subtle variation of spiral ellipticity was seen in Mo doped $MnWO_4$ by Hardy *et al.* [38], notably the saturation of ellipticity occurring at the same temperature as a dielectric anomaly. So, it seems that size reduction and Mo doping may have a similar effect on the ground state. Mo doping can introduce random site-by-site volume anisotropy that destroys the anisotropy driven AF1 ground state and size reduction introduces a surface anisotropy that is different than the volume anisotropy that stabilizes the AF1 state. The notion of surface anisotropy or disorder anisotropy affecting the magnetic ground state is further supported by the tilt angle of the spiral plane with respect to the a axis; 12 deg for S1, and 26 deg for S3, while the value for bulk $MnWO_4$ is 37 deg.

The length of the magnetic moment in the studied series can also be quantified. The magnitude of $C1$, $C2$, and $C3$ gives an upper limit on the modulating moment. Quantification begs a brief return to the moment determination. There are clear local minima in χ^2 and R_{mag}, Fig. 13, but the non-Gaussian shapes of the minima show a strong parameter covariance. The model used has greater sensitivity to the moment length than direction, although both have a clear effect on the goodness of fit. For example, fits forcing $C1 = C2 = C3$ give a similar $|m_{tot}|$, but result in significantly worse goodness of fit parameters. The sample dependence of $|m_{tot}|$ is shown in Table IV.

In all three samples, the magnetic domains are refined to be smaller than the structural domains. The magnetic domain sizes of around 19 nm for S2 and 14 nm for S3 coincide with dimensions of the shortest edge of the nuclear domain, which seems to be the main limiting factor. A different picture is observed in the case of S1, where the magnetic domain size of 7 nm is nearly half of the 16 nm obtained for the nuclear part. The 7 nm (70 Å) size is equivalent to about six magnetic unit cells along the b direction (from the propagation vector and lattice parameters the magnetic cell is $\approx 25 \times 12 \times 10$ Å^3. Such halving of the magnetic coherence length may indicate the presence of two magnetic domains in one crystallite or an influence of a local structural disorder that disrupts the magnetic order at longer distances.

Although we do not explicitly observe the AF3 phase, it may simply have been missed due to the temperature and momentum space that was interrogated in this work. Even in the bulk, the AF3 seems to exist as a precursor to AF2 in a narrow region of magnetic field and temperature. It is also possible that the nanoscale (and potential disorder) smears out the magnetic transition, thereby overlapping the two separate

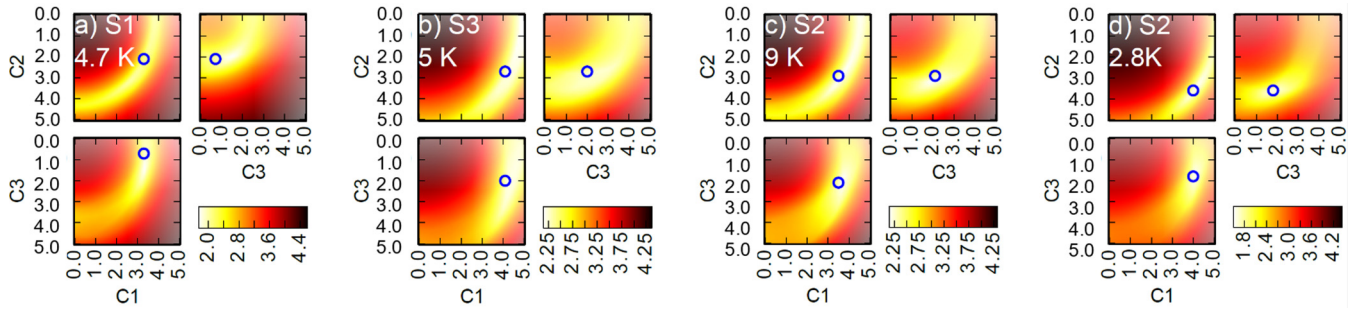

FIG. 13. Maps of $\log(R_{mag})$ around the χ^2 minimum from reported Rietveld refinements. The values of the minima are denoted by open blue circles.

second order phase transition parameters associated with $\boldsymbol{\tau 1}$ and $\boldsymbol{\tau 2}$ irreducible representations that are discernible in large domain samples.

The obtained values of the total moment m_{tot} reported in Table IV are larger than the nominal value of 5 μ_{B} for spin only Mn^{2+}. However, within the 3σ limits and taking into account the fit correlations (Fig. 13) it cannot be inferred that this result does not agree with $S = 5/2$ state of Mn.

V. CONCLUSIONS

This low temperature neutron study of nanosized $MnWO_4$ shows one clear transition to a long-range ordered structure that depends on particle size. The commensurate magnetic AF1 phase was not observed down to 2.8 K in all samples studied and the Rietveld refinements of the incommensurate magnetic structures for all three samples are most consistent with the AF2 phase, with a nonzero magnetic component along the *b* axis. SQUID data shows an additional transition at around 8 K which could be only corroborated by neutron scattering for S2 and is weakly present in S3. This transition studied in detail for S2 is connected with a sudden, over 30%, increase in the value of the magnetic moment component along the *b* axis.

For all samples, the magnetic coherent domain size (between 7 and 16 nm) is smaller than the crystallographic domain (around 25 nm). The smallest magnetic domain ($\approx$ 7 nm) is observed for S1, synthesized at 130 °C, which possesses the highest deviation of the propagation vector from the commensurate values as well as the lowest values of the ordered magnetic moment. Doping with Mo increases the higher transition temperature from 12.1 to 13.6 K, decreases the deviation of the propagation vector from the commensurate point but it does not change the ordered magnetic moment.

ACKNOWLEDGMENTS

The work was supported by the Polish State Committee for Scientific Research (project register No. N N202 260939). We acknowledge the support of the National Institute of Standards and Technology, U. S. Department of Commerce, in providing the neutron research facilities used in this work and support for P.Z. under NIST Guest Researcher program. Certain commercial equipment, instruments, or materials (or suppliers, or software, etc.) are identified in this paper to foster understanding. Such identification does not imply recommendation or endorsement by the National Institute of Standards and Technology, nor does it imply that the materials or equipment identified are necessarily the best available for the purpose.

[1] T. Kimura, S. Ishihara, H. Shintani, T. Arima, K. T. Takahashi, K. Ishizaka, and Y. Tokura, Nature (London) **426**, 55 (2003).
[2] G. Lautenschlager, H. Weitzel, T. Vogt, R. Hock, A. Bohm, M. Bonnet, and H. Fuess, Phys. Rev. B **48**, 6087 (1993).
[3] A. H. Arkenbout, T. T. M. Palstra, T. Siegrist, and T. Kimura, Phys. Rev. B **74**, 184431 (2006).
[4] O. Heyer, N. Hollmann, I. Klassen, S. Jodlauk, L. Bohatý, P. Becker, J. A. Mydosh, T. Lorenz, and D. Khomskii, J. Phys. Condens. Matter **18**, L471 (2006).
[5] K. Taniguchi, N. Abe, H. Umetsu, H. A. Katori, and T. Arima, Phys. Rev. Lett. **101**, 207205 (2008).
[6] H. Katsura, N. Nagaosa, and A. V. Balatsky, Phys. Rev. Lett. **95**, 057205 (2005).
[7] I. V. Solovyev, Phys. Rev. B **87**, 144403 (2013).
[8] H. Sagayama, K. Taniguchi, N. Abe, T. H. Arima, M. Soda, M Matsuura, and K. Hirota, Phys. Rev. B **77**, 220407 (2008).
[9] T. Finger, D. Senff, K. Schmalzl, W. Schmidt, L. P. Regnault, P. Becker, L. Bohaty, and M. Branden, J. Phys. Conf. Ser. **211**, 012001 (2010).
[10] F. Ye, R. S. Fishman, J. A. Fernandez-Baca, A. A. Podlesnyak, G. Ehlers, H. A. Mook, Y. Wang, B. Lorenz, and C. W. Chu, Phys. Rev. B **83**, 140401(R) (2011).
[11] S. H. Park, B. Mihailova, B. Pedersen, C. Paulmann, D. Behal, U. Gattermann, and R. Hochleitner, J. Magn. Magn. Mater. **394**, 160 (2015).
[12] H. Dachs, H. Weltzel, and E. Stoll, Solid State Commun. **4**, 473 (1966).
[13] A. Poole, P. J. Brown, and A. S. Wills, J. Phys. Conf. Ser. **145**, 012074 (2009).
[14] H. W. Yu, X. Li, M. F. Liu, L. Lin, Z. B. Yan, X. H. Zhou, and J. M. Liu, J. Phys. Condens. Matter **26**, 305901 (2014).
[15] K. Taniguchi, N. Abe, H. Sagayama, S. Otani, T. Takenobu, Y. Iwasa, and T. Arima, Phys. Rev. B **77**, 064408 (2008).
[16] I. Urcelay-Olabarria, J. M. Perez-Mato, J. L. Ribeiro, J. L. García-Muñoz, E. Ressouche, V. Skumryev, and A. A. Mukhin, Phys. Rev. B **87**, 014419 (2013).
[17] D. Niermann, C. P. Grams, M. Schalenbach, P. Becker, L. Bohatý, J. Stein, M. Braden, and J. Hemberger, Phys. Rev. B **89**, 134412 (2014).
[18] M. Maczka, M. Ptak, M. Kurnatowska, L. Kepinski, P. E. Tomaszewski, and J. Hanuza, J. Solid State Chem. **184**, 2446 (2011).
[19] J. Ungelenk, M. Speldrich, R. Dronskowski, and C. Feldmann, Solid State Sci. **31**, 62 (2014).
[20] S.-J. Chen, X.-T. Chen, Z. Xue, J.-H. Zhou, J. Li, J.-M. Hong, and X.-Z. You, J. Mater. Chem. **13**, 1132 (2003).
[21] S. G. Bahoosh and J. M. Wesselinowa, J. Appl. Phys. **111**, 083906 (2012).
[22] L. Meddar, M. Josse, M. Maglione, A. Guiet, C. La, P. Deniard, R. Decourt, Ch. Lee, Ch. Tian, S. Jobic, M.-H. Whangbo, and Ch. Payen, Chem. Mater. **24**, 353 (2012).
[23] M. Maczka, M. Ptak, A. Pikul, L. Kepinski, P. E. Tomaszewski, and J. Hanuza, Vibrational Spectrosc. **58**, 163 (2012).
[24] J Ungelenk, S. Roming, P. Adler, W. Schnelle, J. Winterlik, C. Felser, and C. Feldmann, Solid State Sci. **46**, 89 (2015).
[25] N. Hollmann, Z. Hu, T. Willers, L. Bohatý, P. Becker, A. Tanaka, H. H. Hsieh, H.-J. Lin, C. T. Chen, and L. H. Tjeng, Phys. Rev. B **82**, 184429 (2010).
[26] R. P. Chaudhury, B. Lorenz, Y. Q. Wang, Y. Y. Sun, and C. W. Chu, Phys. Rev. B **77**, 104406 (2008).
[27] H. M. Rietveld, J. Appl. Crystallogr. **2**, 65 (1969).

[28] J. Rodriguez-Carvajal, (2001) Recent Developments of the Program FULLPROF, in Commission on Powder Diffraction (IUCr). Newsletter **26**, 12 (http://journals.iucr.org/iucr-top/comm/cpd/Newsletters/).
[29] P. Thompson, D. E. Cox, and J. B. Hastings, J. Appl. Crystallogr. **20**, 79 (1987).
[30] P. W. Stephens, J. Appl. Crystallogr. **32**, 281 (1999).
[31] M. Jarvinen, J. Appl. Crystallogr. **26**, 527 (1993).
[32] Yu. A. Izyumov, V. E. Naish, and R. P. Ozerov, *Neutron Diffraction of Magnetic Materials* (Consultants Bureau, New York, 1991).
[33] A. S. Wills, Physica B **276**, 680 (2000).
[34] See Supplemental Material at http://link.aps.org/supplemental/10.1103/PhysRevB.95.174427 for the room temperature XRD, coherent domain size obtained from the analysis of peak broadening, basis vectors for NPD refinements, and χ^2 and R_{mag} maps of magnetic structures.
[35] K. Momma and F. Izumi, J. Appl. Crystallogr. **44**, 1272 (2011).
[36] R. T. Azuah, L. R. Kneller, Y. Qiu, P. L. W. Tregenna-Piggott, C. M. Brown, J. R. D. Copley, and R. M. Dimeo, J. Res. Natl. Inst. Stand. Technol. **114**, 341 (2009).
[37] R. D. Shannon, Acta. Crystallogr. Sect. A **32**, 751 (1976.]
[38] V. Hardy, C. Payen, F. Damay, L. Meddar, M. Josse, and G. Andre, J. Phys. Condens. Matter **28**, 336003 (2016).